The Photothermal Stability of PbS Quantum Dot Solids

Rachelle Ihly, Jason Tolentino, Yao Liu, Markelle Gibbs, and Matt Law*

Department of Chemistry, University of California, Irvine, California 92697, United States

ABSTRACT We combine optical absorption spectroscopy, *ex situ* transmission electron microscopy (TEM) imaging, and variable-temperature measurements to study the effect of ultraviolet (UV) light and heat treatments on ethanedithiol-treated PbS quantum dot (QD) films as a function of ambient atmosphere, temperature, and QD size. Film aging occurs mainly by oxidation or ripening and sintering depending on QD size and the presence of oxygen. We can stop QD oxidation and greatly suppress ripening by infilling the films with amorphous Al_2O_3 using room-temperature atomic layer deposition (ALD).

KEYWORDS: quantum dots · nanocrystals · PbS · photothermal stability · solar cells

Thin films of IV–VI (MX, where M = Pb, Sn and X = S, Se, Te) quantum dots (QDs) represent a novel class of granular electronic materials of great promise for a variety of applications, including high-performance field-effect transistors (FETs),[1–7] ultrasensitive photodetectors,[8–11] infrared light-emitting diodes and lasers,[12–16] metamaterials,[17–19] and solar cells,[20–33] but these QD solids are inherently metastable materials prone to oxidative and photothermal degradation driven by their large surface-to-volume ratios and high surface energies, and poor environmental stability limits their use in practical devices.[22,23,34,35] To date, most investigations of IV–VI QD stability have focused on the spontaneous, thermally activated oxidation of PbX QDs. These studies show that exposing PbX QD solutions or solids to oxygen rapidly decreases the physical and electronic size of the QDs and increases their energy gap, resulting in excitonic blue shifts in absorption and emission spectra.[36–40] Brief oxygen exposures dramatically increase the hole concentration and electrical conductivity of electronically coupled PbX QD solids.[22,41–44] Recent studies of 1,2-ethanedithiol (EDT)-capped PbSe QD films suggest that oxidation is a two-stage process consisting of (*i*) fast (within seconds) oxidative desorption of EDT and adsorption of O_2 and H_2O species that dope the QD films with holes and increase conductivity, followed by (*ii*) slow (over months) formation of an oxide shell around each QD that gradually decreases film conductivity.[44,45] Oxidation is usually detrimental to PbX QD devices because it decreases luminescence yields, scrambles doping profiles,[4] introduces traps,[34,39] alters the properties of electronic junctions,[22] and causes other unwelcome changes.

Less well studied than oxidation is the impact of thermal, photo, and electrical stressors on the morphology and optical and electronic properties of PbX QD systems in different environments. QDs in solutions and solids are expected to ripen and sinter at temperatures far below the threshold temperatures for the corresponding bulk materials, driven mainly by reduction of surface energy. The temperature at which a QD solid begins to sinter should depend on QD size, packing, surface ligands, and the mobility of both the QD surface atoms and the QDs themselves. Removal of the capping ligands increases the QD surface energy and enables direct QD–QD contact, both of which promote coalescence and grain growth. Recently, van Huis *et al.* demonstrated that hexylamine-capped PbSe QDs rotate, translate, and fuse (sinter) at surprisingly low temperatures (~100 °C) during *in situ* TEM heating experiments.[46,47] X-ray scattering studies show that 3D superlattices of 6–8 nm diameter, oleate-capped PbS and PbSe QDs start to sinter at ~230 and ~150 °C, respectively.[42,48,49] Whereas heating QD films in oxygen accelerates oxidation and causes blue shifts in optical spectra (*i.e.*, smaller QDs), heating in inert atmosphere results in Ostwald ripening, sintering, and red shifts in optical spectra (larger QDs).[42,50,51] The dense network of surfaces and grain boundaries within a QD solid is expected to promote the diffusion of ligands, QD surface atoms, and even the QDs themselves, particularly during long-term continuous exposures to light, heat, and electric fields (conditions typical for solar cells, for example). Local heating during photothermal (*i.e.*, light plus heat) soaking may result in the desorption of ligands

* Address correspondence to matt.law@uci.edu.

Received for review July 25, 2011 and accepted September 3, 2011.

Published online September 03, 2011
10.1021/nn2033117

© 2011 American Chemical Society

and adatoms, interdiffusion of species across heterojunctions, and chemical reactions within a QD solid. Motion by any of these mechanisms, if unintended, can destroy the functionality of a QD device. Basic studies are needed to elucidate the most important mechanisms of degradation and to develop robust countermeasures if IV–VI QD solids are to become technologically significant materials.

Here we combine optical absorption spectroscopy, *ex situ* transmission electron microscopy (TEM) imaging, and variable-temperature methods to study the effect of UV light and heat soaking on EDT-treated PbS QD films as a function of QD size, ambient atmosphere (aerobic or inert gas), and temperature. We focus on PbS QDs rather than cadmium or zinc chalcogenides because IV–VI QD solids have ideal band gaps for use in multiple exciton generation (MEG) enhanced solar cells. Furthermore, PbX QD solids show high carrier mobilities and conductivities as well as good prospects for exhibiting the long carrier diffusion lengths needed for efficient solar cells. Facile charge transport *via* hopping or mini-band conduction[52] is favored in PbS QDs by the synergy of a large exciton Bohr radius, high densities of states, and high dielectric constant, which together result in strong inter-QD electronic coupling and the minimization of Coulomb blockade and Anderson localization effects. Finally, we were inspired to study PbS rather than PbSe QDs by recent reports of exceptionally stable solar cells based on small (2–3 nm) PbS QDs.[30,35]

RESULTS

Sample Preparation. Figure 1 shows basic structural and optical characterization of the colloidal PbS QDs and QD films used in this study. We employed a modified literature procedure[53] to synthesize three large batches of PbS QDs having average diameters of 2.9 ± 0.3, 5.0 ± 0.6, and 7.0 ± 0.7 nm as determined by TEM. These diameters correspond to a first exciton absorption energy of 1.31, 0.91, and 0.72 eV, respectively, which agree well with published size–band gap curves for oleate-capped PbS QDs in tetrachloroethylene solution.[54] Absorption peak widths (full width at half-maximum, fwhm), which are directly proportional to the size polydispersity of a QD sample, are 134, 88, and 74 meV for the small, medium, and large QDs in solution. Photoluminescence (PL) emission peaks occur at 1.19 eV (fwhm = 210 meV) and 0.87 eV (fwhm = 120 meV) for the small- and medium-sized QDs (emission from the large QDs was too red for our detector).

QD films were prepared using a layer-by-layer dip coating process[41] in which EDT removes the electrically insulating oleate capping ligands that originally solubilize the QDs to yield EDT-capped, electronically coupled PbS QD films with a thickness of 90 ± 10 nm. Similar EDT-treated QD films have been employed in the more efficient QD solar cells reported to date.[55] Plan view and cross-sectional scanning electron microscopy (SEM) images show that the films are uniform over large areas but possess significant surface porosity and roughness (Figure 1e). The first exciton peak of freshly made EDT-treated QD films is red-shifted relative to QDs in solution because of the increased dielectric constant and substantial electronic coupling in EDT-treated films.[41,42] Upon film formation, we observed average red shifts of 85, 50, and 15 meV for the 3, 5, and 7 nm QDs, respectively. The peak width varies by 5–10 meV between films, but there is no average difference in peak width for QDs in solution and in the solid state.

PbS QD films ripen, sinter, and oxidize when exposed to UV light and heat for extended periods of time (*vide infra*). To improve film stability, we use room-temperature atomic layer deposition (ALD) to infill the internal pore network of these films with amorphous alumina and then cap the films with a thin alumina overcoating. ALD is a stepwise chemical vapor deposition method for making thin conformal films on nonplanar substrates with submonolayer thickness control, and low-temperature ALD is uniquely suited to growing high-quality films on delicate, topologically complicated substrates.[56–63] ALD has been used to fill the pores of TiO_2 NC films consisting of NCs with diameters as small as 10 nm.[64] More recently, ZnO deposited by ALD at 100 °C was shown to penetrate CdSe QD films and increase film conductivity and carrier mobility.[65]

Figure 1e shows typical SEM images of a PbS QD film after deposition of 18 nm of ALD alumina at 27 °C. Elemental depth profiling with X-ray photoelectron spectroscopy (XPS) confirms that the first few nanometers of alumina coat the accessible internal surface of the film to make a three-dimensional PbS/Al_2O_3 inorganic nanocomposite (see Figure S1 in the Supporting Information). Additional ALD deposition eventually seals off the pore network and yields a capping layer of alumina on the external surface of the film. For the purposes of this study, the ALD alumina coating is intended to serve two functions: (*i*) the infilling inhibits atomic and molecular diffusion that causes QD ripening and sintering, and (*ii*) the overcoating acts as a gas diffusion barrier to prevent QD oxidation. The ALD matrix can also exert electronic effects on a QD film (*e.g.*, surface state passivation, tunnel barrier lowering), and this will be the subject of future reports.

Photothermal Aging. Films were placed on an upended hand-held UV lamp and illuminated with 365 nm light continuously for 1 month (1.4 mW cm^{-2} at the sample position, with illumination through the glass substrate). This UV power density is about one-third of that of the full sun AM1.5 G spectrum (~4.6 mW cm^{-2} integrated over 280–400 nm). The films were warmed naturally to ~50 °C by the hot lamp

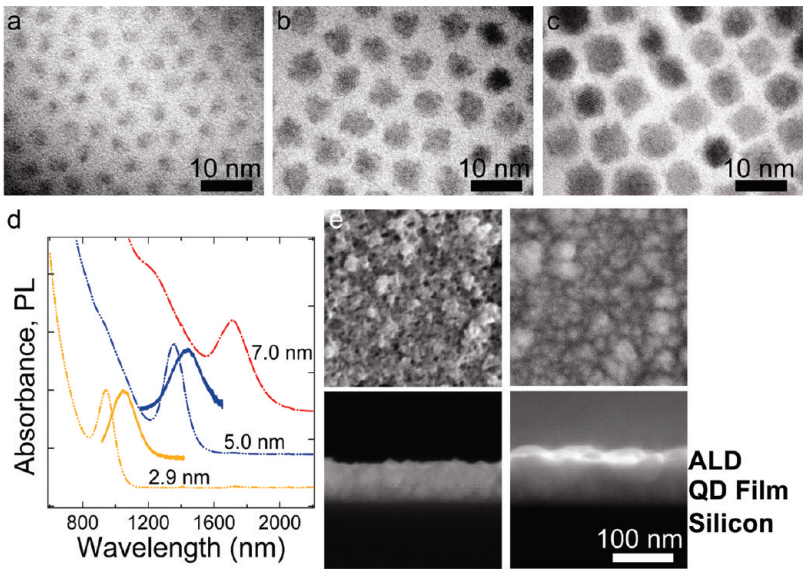

Figure 1. Characterization of the PbS QDs used in this study. TEM images of (a) 2.9 ± 0.3 nm, (b) 5.0 ± 0.6 nm, and (c) 7.0 ± 0.7 nm PbS QDs. Scale bars = 10 nm. (d) Optical absorption and PL emission spectra of the three QD samples in tetrachloroethylene solution. The first exciton absorption energy is 1.31 eV (fwhm = 134 meV), 0.91 eV (fwhm = 88 meV), and 0.72 eV (fwhm = 74 meV), respectively. The PL energy is 1.19 eV (fwhm = 210 meV) and 0.87 eV (fwhm = 120 meV) for the 2.9 and 5.0 nm QDs, respectively. (e) Top-down and cross-sectional SEM images (on ITO and Si substrates, respectively) of 7 nm QD films before and after ALD treatment (18 nm alumina deposited at 27 °C). These films are similar in thickness and morphology to the films on glass used in this study (films on glass proved intractable to image).

during the UV soaking treatments. We refer to the combination of light and heat exposure as photothermal soaking.

Integrating sphere measurements and an optical model were used to determine the UV absorption lengths and absorption profiles of the films at λ = 365 nm (see Figure S2).[24] The measured absorption lengths, $(\alpha_{365})^{-1}$, are 27, 29, and 36 nm for layers of the small, medium, and large QDs, respectively, which is short compared to the 90 nm thickness of the films. Optical modeling of 100 nm thick QD films on glass reveals Beer–Lambert-type absorption profiles with a weak interference structure causing a broad absorption minimum about 75 nm into the films. The QDs at the top of the films experience only 2–10% of the UV intensity seen by QDs at the surface of the glass substrate. This highly non-uniform illumination probably exacerbates the excitonic peak broadening we observe during photothermal soaking, as discussed below.

Figure 2a–c presents typical absorption spectra for three different films of 5 nm QDs as a function of photothermal soaking time in nitrogen and air (365 nm light at 50 °C). Films soaked in nitrogen (glovebox with <5 ppm O_2 and H_2O) exhibit a slow, steady red shift and broadening of their first exciton peak, with a total red shift of 46 meV and broadening of 39 meV after 1 month. Time traces of the peak energy and width (Figure 2d) suggest that the spectral changes have not stopped after 1 month. In contrast, films in air show a rapid and dramatic blue shift (135 meV) and broadening (74 meV) of the excitonic peak within the first week of soaking, followed by only minor changes thereafter. The exciton is nearly washed out by photothermal soaking in air. Control experiments were performed to ascertain the effects of long-term exposure to nitrogen or air (*i*) without UV light or heat and (*ii*) with heat alone (Figure S3). Films stored in nitrogen in the absence of light and heat showed only a slight red shift (8 meV) and broadening (11 meV), while heat alone caused a slight red shift (8 meV) and significant broadening (28 meV). We therefore conclude that ~85% of the red shift and 25% of the broadening observed in films in nitrogen is caused by the UV flux itself rather than the 50 °C thermal bath. Meanwhile, films stored in air in the absence of light and heat exhibited a 95 meV blue shift and 37 meV broadening, consistent with the spontaneous oxidation of PbS QDs at room temperature, while heating in air caused a slow 128 meV blue shift and 41 meV broadening. On the basis of these results, we believe that none of the blue shift but ~35% of the broadening observed for films in air can be attributed to UV light rather than heating alone. UV illumination certainly intensifies the morphological and chemical changes that occur in the films.

The different aging behavior of films soaked in nitrogen and air implies the action of distinct aging processes. Films in nitrogen red shift because heating promotes diffusion which, in the absence of oxygen, causes the QDs to change shape, ripen, and fuse (sinter), thereby increasing the average QD size (and size distribution) and relaxing the overall quantum confinement of the system. Such diffusion can occur even at room temperature. Some of the red shift may also result from relaxation of the EDT ligands

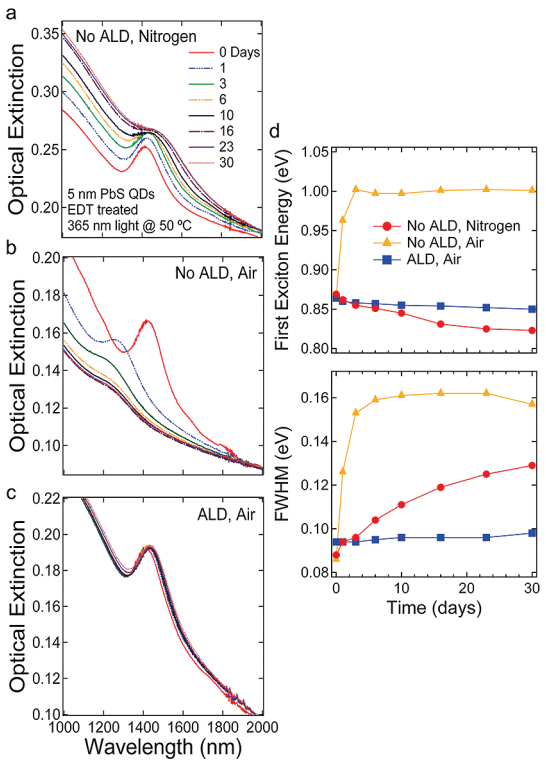

Figure 2. UV photothermal soaking of films of 5 nm PbS QDs in air and nitrogen. Typical optical absorption spectra as a function of time exposed to UV light (1.4 mW cm^{-2} at 365 nm) and heat (50 °C) for an untreated QD film in (a) nitrogen and (b) air, as well as (c) an ALD-infilled film in air (18 nm alumina deposited at 27 °C). The traces in each graph are offset to overlay at λ = 2000 nm. (d) Time traces of the first exciton peak energy and peak width for the three films. The first exciton peak of films in air (nitrogen) blue shifts (red shifts) and broadens considerably. The spectra of ALD-infilled films exhibit only a slight red shift (~12 meV) over the first 30 days of photothermal soaking and almost zero peak broadening (~4 meV, compared to ~70 meV for uncoated films in air).

(solvatochromism), desorption of EDT molecules, or subtle decreases in inter-QD spacing during soaking, but these effects are expected to be minor compared to ripening and sintering when films are heated or exposed to UV light. Films in nitrogen show a steady increase in broad-band absorbance as the average band gap decreases with soaking time (Figure 2a). Soaking a film in air activates diffusion too, but it also enhances the rate of surface oxidation reactions that produce oxidized QDs with smaller PbS cores and greater electronic confinement. The competition between ripening/sintering and oxidation determines whether a QD film exhibits a net red shift or blue shift during photothermal soaking. The 5 nm QD films show a steady and considerable blue shift in air, indicating that oxidation is the dominant process in these films. The considerable decrease in broad-band absorbance for films soaked in air (Figure 2b) is a result of the increased average band gap of the QDs and conversion of a fraction of the film volume to surface oxides (which have larger band gaps).

Whereas the excitonic peak shifts one way or the other depending on the ambient gas and other conditions, the peak width—which is proportional to the QD size distribution—consistently increases because (*i*) ripening, sintering, and oxidation proceed unevenly within the films, and (*ii*) the UV flux is non-uniform across the thickness of the films (as mentioned above). Both of these effects increase the QD polydispersity.

We can use the known size–band gap relationship for PbS QDs (Figure S4) to picture the morphological changes that result from photothermal soaking.[54] This is easy to do in nitrogen because ripening/sintering is the main process causing large changes in peak energy and width, so red shifts can be plausibly related to increased QD size. We estimate that the 46 meV red shift observed for 5 nm QD films UV-soaked in nitrogen corresponds to a 0.4 nm increase in the average QD size. If this size increase occurs by a combination of Ostwald ripening and sintering, these films should consist of relatively polydisperse, mostly spheroidal QDs mixed with some fraction of sintered ("necked") QDs.

This approach is not as useful for films soaked in air because red shifts from ripening/sintering are convolved with blue shifts from oxidation, making it impossible to assign peak shifts to size changes of the PbS QD cores alone; a small peak shift could indicate that a film is either unchanged or sintered and oxidized to equal degrees. If we assume that the 5 nm QD films UV soaked in air experience only oxidation, then the 135 meV blue shift corresponds to a 0.9 nm decrease in the average size of the PbS cores. The neglect of both ripening/sintering and the finite band gaps of the surface oxides (PbO, $PbSO_4$, *etc.*) makes this a lower estimate. Despite the limitations, we can successfully use optical spectra to deduce the general morphological changes of films soaked in air. We picture these films as consisting of polydisperse, irregularly shaped QDs that are heavily contaminated by surface oxides and lightly sintered. This morphology is indeed observed in TEM images of 7 nm QDs soaked in UV in air (see below).

ALD infilling of the 5 nm QD films greatly suppresses photothermal degradation. ALD-infilled films soaked in air showed only a 14 meV red shift and 4 meV broadening after 1 month, similar to the shifts observed with "no light, no heat" control samples in nitrogen (Figure S3). The slight red shift suggests that the ALD layer stops oxidation—the film behaves like it is in nitrogen, not air—but does not completely inhibit diffusion within the bulk of the film, either because pockets of the interstitial network are poorly infilled or some diffusion occurs in spite of the ALD coating (for example, at QD–QD necking points that are too narrow for ALD precursor molecules to access). Regardless of this small red shift, it is clear that our ALD infilling method can produce QD solids with greatly enhanced photothermal stability.

TABLE 1. Effect of Thermal and Photothermal Treatments on Excitonic Peak Energy, Peak Width, Average Diameter, and Diameter Distribution of PbS QD Films[a]

QD size (nm)	gas	treatment	$\Delta E_{1Sh-1Se}$ (meV)	Δfwhm (meV)	$d \pm \Delta d$ (nm)[d]
2.9 ± 0.3	N_2	no UV, −80 °C	−2	1	2.9 ± 0.3
	N_2	no UV, no heat	−22	12	2.9 ± 0.4
	N_2	heat only	−42	50	3.0 ± 0.5
	N_2	UV	−100	185	3.3 ± 1.2
	air	no UV, no heat	146	24	2.5 ± 0.3
	air	heat only	207	47	2.4 ± 0.3
	air	UV	124, −86[b]	41, −8[b]	2.7 ± 0.3
	air	*ALD, UV*	**−90**	**30**	**3.3 ± 0.5**
5.0 ± 0.6	N_2	no UV, no heat	−8	11	5.0 ± 0.7
	N_2	heat only	−8	28	5.0 ± 0.9
	N_2	UV	−46	39	5.4 ± 1.2
	air	no UV, no heat	95	37	4.3 ± 0.7
	air	heat only	128	41	4.2 ± 0.7
	air	UV	135	74	4.1 ± 1.0
	air	*ALD, UV*	**−14**	**4**	**5.1 ± 0.6**
7.0 ± 0.7	N_2	no UV, no heat	−7	10	7.1 ± 0.8
	N_2	heat only	−6	15	7.1 ± 0.9
	N_2	UV	−16	32	7.3 ± 1.2
	air	no UV, no heat	54	24	6.3 ± 0.8
	air	heat only	77	27	5.9 ± 0.8
	air	UV	>156[c]	>105[c]	<5.2 ± >1.6
	air	*ALD, UV*	**−6**	**3**	**7.1 ± 0.7**

[a] All data after 1 month of soaking. "UV" = 1.4 mW cm^{-2} of 365 nm light (this warms the films to ~50 °C). "Heat" = 50 °C. "ALD" = 18 nm of alumina deposited at 27 °C. [b] Spectral changes not monotonic. [c] Peak indistinct after 4 days. [d] Effective size changes from PbS QD TEM sizing curve (Figure S4).[54] These estimates attribute all optical shifts to size changes, ignoring changes in dielectric constant, coupling energy, and other factors, as well as the band gap of any oxide surface layer. See text for details.

We now summarize the behavior of the larger (7 nm) and smaller (3 nm) QD films. The raw data are presented in Figures S5−S8 and compiled in Table 1 along with the results from the 5 nm QDs. Table 1 also lists the estimated average size and size distribution of each sample after treatment, as determined from the TEM sizing curve (Figure S4). Photothermal soaking of 7 nm QD films in nitrogen results in a 16 meV red shift and 32 meV broadening. Control films in nitrogen show a 7 meV red shift and 10 meV broadening in the absence of light and heat and a 6 meV red shift and 15 meV broadening with heat alone. In air, photothermal soaking causes a very large blue shift (>156 meV) and broadening (>105 meV) that completely washes out the excitonic peak after just 4 days of testing. Control films in air show a 54 meV blue shift and 24 meV broadening without light and heat, while heat alone results in a 77 meV blue shift and 27 meV broadening. ALD-infilled 7 nm QD films are extremely stable in air, showing only a 6 meV red shift and almost zero broadening (~3 meV) after 1 month of UV exposure.

Photothermal soaking of 3 nm QD films in nitrogen results in a 100 meV red shift and 185 meV broadening. Control films in nitrogen show a 22 meV red shift and 12 meV broadening in the absence of light and heat and a 42 meV red shift and 50 meV broadening with heat alone. Photothermal soaking in air causes a rapid and pronounced blue shift (124 meV), followed by a slow red shift of 86 meV. The change in peak width is similarly nonmonotonic: an initial broadening of 41 meV is followed by noticeable narrowing (8 meV) over the course of the month. Control films in air show a monotonic 146 meV blue shift and 24 meV broadening without light and heat, while heat alone results in a 207 meV blue shift and 47 meV broadening. ALD-infilled 3 nm QD films show a substantial red shift (90 meV) and some broadening (30 meV).

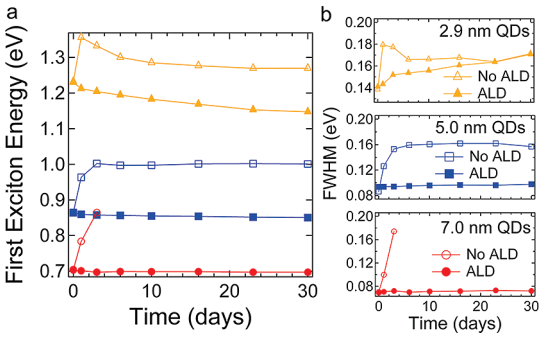

Figure 3. Comparative photothermal aging in air for the three QD sizes. (a) First exciton energy *versus* time in air. Open symbols are bare films, and closed symbols are ALD-infilled films (18 nm alumina at 27 °C). All samples were exposed to 365 nm UV light at 50 °C in air. The exciton peak of unprotected films of the largest QDs (open circles) was completely washed out after 4 days of photothermal soaking. (b) Peak width *versus* time in air. The legends in (b) apply to (a).

It is clear that ALD infilling is least effective at preventing red shifting and broadening of the smallest QDs. Figure 3 shows this explicitly by comparing the photothermal aging behavior of bare and ALD-infilled films of the three QD sizes. Whereas infilled 7 and 5 nm QD films show minimal changes in peak energy and peak width, the 3 nm QD films red shift and broaden considerably. This is caused by incomplete infilling of the exceedingly narrow interstitial spaces in the 3 nm QD films. We can estimate the size of these interstitial voids by modeling the films as a close-packed array of spheres with a center-to-center distance of 3.5 nm (2.9 + 0.6 nm to accommodate the EDT ligands). The largest interstitial sites in such a film are approximately 1.5 nm in diameter, not much larger than the trimethylaluminum molecules used in the ALD process (approximate TMA dimensions: 7.4 Å × 7.4 Å × 4.2 Å).[66] Although our QD films are not close-packed and the largest interstitial spaces are certainly bigger than estimated here, it is reasonable to expect the diffusion of ALD precursors to be inhibited by the particularly tortuous pathways within films of the smallest QDs.

Figure 3 also shows that the aging behavior of the bare films in air depends strongly on QD size. The large QDs show the largest blue shift and broadening,

resulting in complete washout of the excitonic peak, while the medium-sized QDs exhibit a moderate blue shift and broadening and the small QDs first blue shift and then red shift. To separate the effects of UV exposure and heat exposure, Figure 4 compares the photothermal and thermal aging behavior at nominally the same average temperature (50 °C) for all three QD sizes. We observe that, relative to heat alone, UV illumination causes an increased blue shift for the large QDs, little change for the medium QDs, and a reversal of the initial blue shift for the small QDs.

To explain these results, it is useful to re-emphasize that shifts in peak energy reflect the net, ensemble-averaged outcome of processes that cause blue shifts and red shifts in the QD films. In air, blue shifts result mainly from oxidation (leading to decreased QD core diameters, lower dielectric constants, and less electronic coupling), while red shifts arise from ripening and sintering (resulting in increased QD diameters, higher local dielectric constants, and greater coupling). QD films in air undergo ripening/sintering and oxidation simultaneously, so the overall peak shift depends on the competition between these two relatively complicated processes.

UV illumination can promote thermally activated processes such as oxidation and ripening/sintering by at least three distinct mechanisms: (*i*) generating electrons and holes capable of participating in chemical reactions at the surface of the QDs; (*ii*) creating localized, transient temperature spikes ("hotspots") from the cooling and recombination of hot carriers; and (*iii*) raising the average steady-state film temperature above 50 °C *via* photon absorption. The first effect should promote surface redox reactions such as oxidation, while the latter two should increase the rate of both oxidation and ripening/sintering within the films.

To test the third mechanism (higher steady-state film temperature), we soaked films at elevated temperatures (65 and 80 °C) in the absence of UV light (Figure 5). These higher-temperature thermal soaks resulted only in larger blue shifts (greater oxidation) for bare QD films. Because increasing the soak temperature does not reproduce the qualitative or quantitative effects of UV illumination seen in Figure 4, we conclude that UV exposure must be doing more than just uniformly heating the films. The likelihood that the UV flux increases film temperature substantially above 80 °C seems low. Therefore, we rule out steady-state film heating as an important effect of UV illumination.

The data in Figure 4 are best explained if UV illumination triggers photo-oxidation (mechanism 1) and hot-spot-induced ripening/sintering (mechanism 2) in a ratio that varies systematically with QD size. Our results show that long-term UV exposure causes net oxidation of large QDs but net sintering of small QDs. This size dependence probably results from the larger thermodynamic driving force for the ripening/sintering of

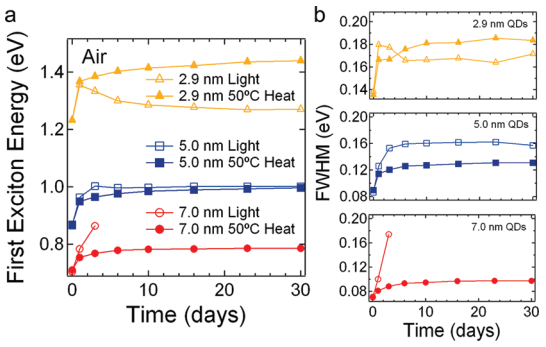

Figure 4. Comparison of thermal and photothermal aging behavior for the three QD sizes (no ALD). (a) First exciton energy *versus* time in air. Open symbols are films exposed to UV light and heat; closed symbols are films exposed to heat alone. (b) Peak width *versus* time in air. The legends in (a) apply to (b).

smaller, higher surface area spheres. If ripening/sintering is favored for smaller QDs but oxidation is independent of size (such that smaller QDs undergo more ripening/sintering as they oxidize), then net peak shifts should be redder for smaller QDs, as observed (Figure 4). In other words, we believe that photo-oxidation occurs about equally for all QD sizes but UV-generated temperature spikes preferentially cause surface diffusion and ripening/sintering of small QDs because of the larger driving force for surface area reduction in small QD films. Thus, UV exposure of 3 nm QDs yields an initial blue shift (oxidation) followed by a marked red shift (ripening/sintering). UV exposure of 5 nm QDs enhances oxidation and ripening/sintering about equally, so these effects cancel and there is little net change compared to thermal soaking alone. Finally, UV exposure of 7 nm QDs enhances oxidation more than ripening/sintering, causing the excitonic peak to blue shift strongly with soaking time.

In contrast to recent reports of remarkable air stability of small PbS QDs in solar cells,[30,35] we observe considerable shifts in the peak energy and width of small (3 nm) QD films for all aging conditions explored in this study (no light or heat, heat only, and UV soaking). Moreover, ALD infilling stops the oxidation but not the ripening/sintering of these films during UV soaking in air. Since the ALD overcoat acts as a gas diffusion barrier in a manner similar to the top metal electrode of a solar cell, it is remarkable that Luther *et al.* found negligible peak shifts in the photocurrent spectra of unencapsulated PbS QD solar cells even after 1000 h of light soaking in air.[30] These differing results may be attributed to important differences in testing conditions: their stability tests were performed at 20 °C using a low-flux sulfur plasma lamp that emits very little UV light, while our ALD-infilled films were tested at 50 °C in relatively strong UV light. Moving forward, it will be interesting to test the stability of PbS QD solar cells at higher temperatures and under intense AM1.5 G illumination.

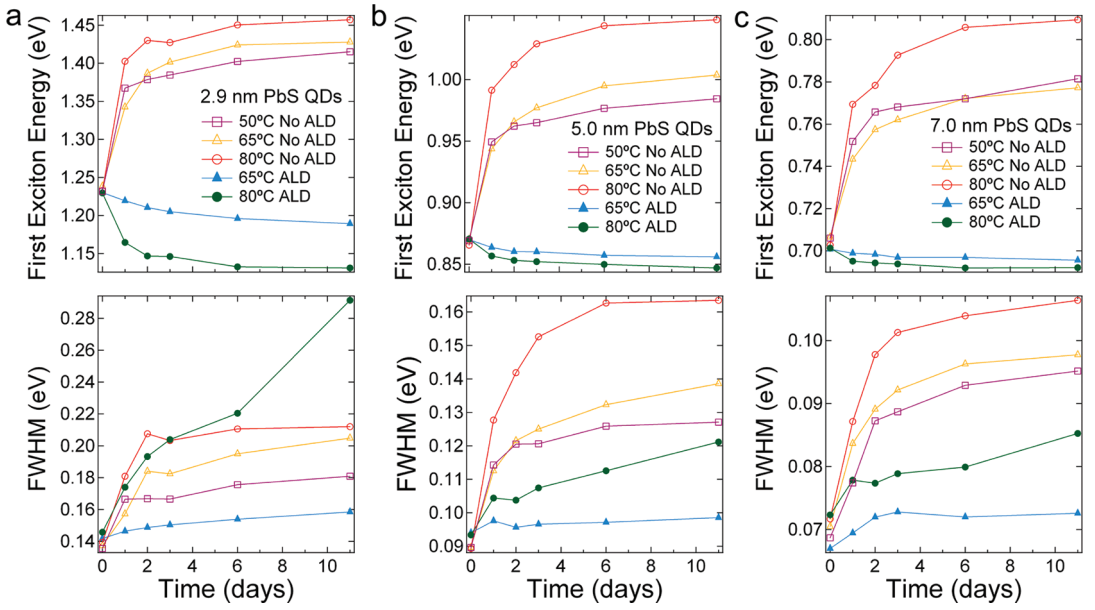

Figure 5. Thermal aging behavior in air at different temperatures. Time traces for (a) 3 nm, (b) 5 nm, and (c) 7 nm QD films. Both uncoated and ALD-infilled films are shown.

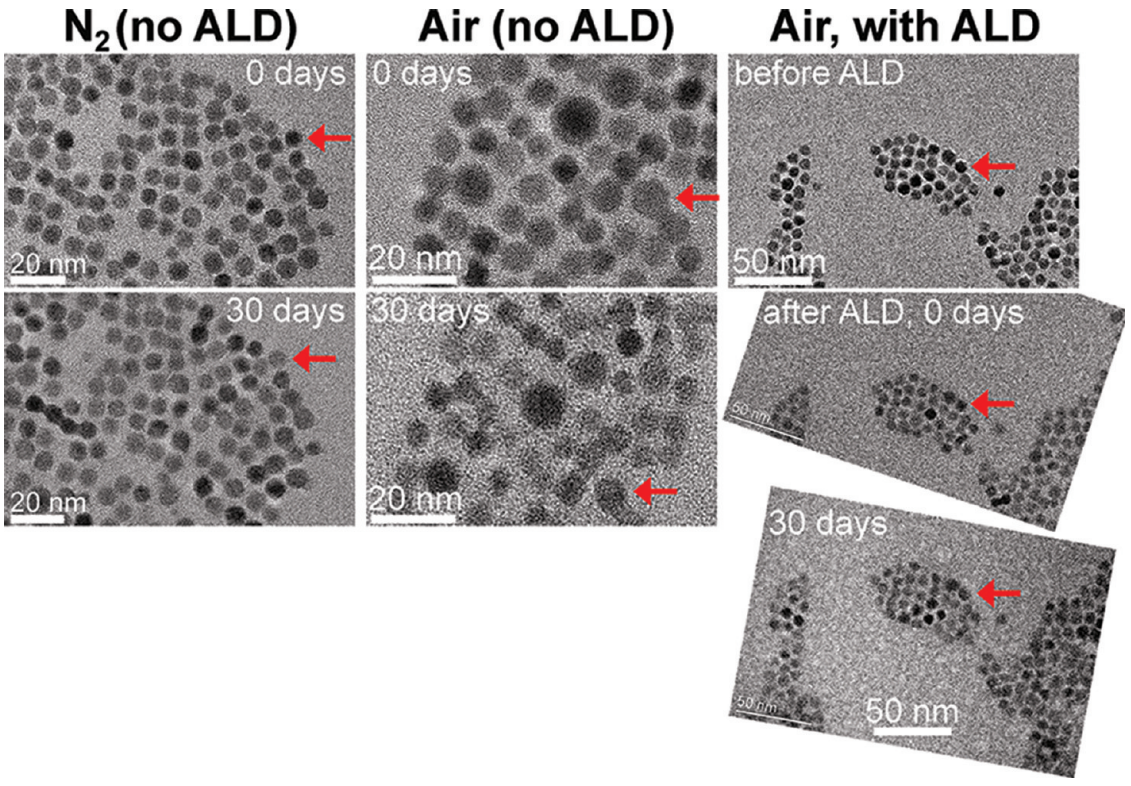

Figure 6. *Ex situ* TEM imaging of UV-soaked QD monolayers. Sample conditions are as follows: (left) nitrogen without ALD; (middle) air without ALD; (right) air with ALD. The red arrows are reference markers for each pair of images. Electron beam damage was negligible in these experiments. However, we observed substantial beam damage of ALD-infilled monolayers at higher magnification. Controls for samples aged in the dark in nitrogen at 193 and 298 K and in air at 298 K can be found in the Supporting Information (Figure S10).

***Ex Situ* TEM Imaging.** We used TEM to directly image QD monolayers before and after photothermal soaking. Although monolayers cannot be expected to age in precisely the same fashion as multilayer QD films, they should provide a qualitatively accurate picture of the morphological changes induced by the various treatments. Samples were prepared on SiO_2 window TEM grids by drying a drop of QD solution followed by

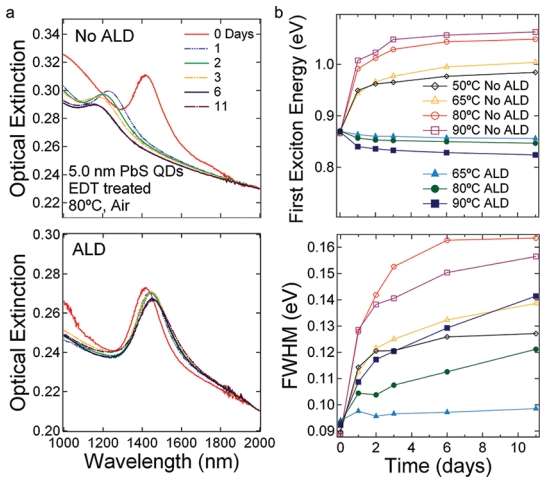

Figure 7. Thermal soaking of films of 5 nm PbS QDs in air. (a) Raw data for EDT-treated QD films soaked at 80 °C in the dark, without and with ALD treatment. (b) Peak energy and width *versus* time for films soaked at 50, 65, 80, or 90 °C for 11 days.

ligand exchange with EDT. We studied only the largest of the three QD sizes (7 nm) because of the difficulty in obtaining useful time series images of the smaller QDs. Figure 6 compares representative images of QD monolayers before and after a month of UV soaking in nitrogen or air without ALD *versus* in air with ALD. The QDs aged in nitrogen lose their faceting (becoming more "diffuse" in shape and size) but do not show obvious ripening or sintering, which is consistent with the small red shift and minor broadening observed in absorption spectra of the corresponding multilayer films (Figure S5). In contrast, the QDs aged in air show marked changes in size and shape and some changes in connectivity (Figures 6 and S9). The average QD diameter appears to shrink by ~0.7 nm, the shapes become more irregular, and the size distribution considerably broadens after photothermal treatment, but the positions of the QDs are nearly unchanged (to within 1−2 nm). It is clear from these images that the QDs both oxidize and ripen in air and, furthermore, that ripening occurs mostly by atomic diffusion between immobile QDs rather than by QD diffusion and aggregation. These morphological changes are qualitatively consistent with the large blue shift and broadening observed in film spectra (Figure S5).

We also imaged QD monolayers immediately before and after the deposition of 18 nm of ALD alumina and again after 1 month of photothermal soaking in air. The presence of the ALD coating leads to a considerable loss of image sharpness (Figure 6). Despite the blurriness of the post-ALD images, we can conclude that the QDs retain their positions and sizes after photothermal soaking, as anticipated from the nearly unchanged absorption spectra of the multilayer films. The ALD coating effectively stops both oxidation and ripening of the QDs (at least at this temperature).

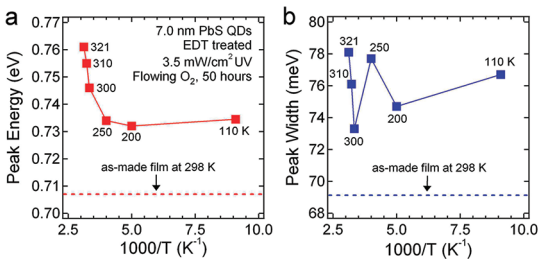

Figure 8. First exciton peak energy and width for films soaked in UV and oxygen for 50 h at various temperatures. (a) Peak energy. (b) Peak width. The values for a film before UV soaking are indicated by the dotted lines. All absorption measurements were performed at room temperature.

High-Temperature Aging. Commercial photovoltaic modules must pass demanding environmental stability tests, including 1000 h soaks at 85 °C and 85% relative humidity (so-called 85/85 damp heat tests). As a prelude to true device testing, we soaked 5 nm QD films at 65, 80, and 90 °C in air in the dark to determine how they respond to elevated temperatures. Figure 7a presents stacked spectra of bare and ALD-infilled films soaked at 80 °C for 11 days, while Figure 7b compiles the time trends in peak energy and width for all samples studied. It is evident from these data that higher temperatures generally cause larger peak shifts and greater broadening, as expected. The small, temperature-dependent red shift and broadening observed with ALD-infilled films indicates that the ALD coating remains an effective oxidation barrier but allows progressively greater ripening and sintering of the QDs at higher temperatures. It is not yet clear how this internal diffusion will affect the electrical properties of the films (conductivity, carrier type and mobility, *etc.*). ALD-infilled films tested at 100 °C showed rapid blue shifting and complete loss of the exciton peak within 1 day, which we interpret as complete structural failure of the ALD matrix caused by chemical reactions between it and the QDs. Better thermal stability may be achievable by using denser ALD alumina coatings deposited at higher temperatures (50−75 °C) or by switching to another ALD material (MgO or SiO_2, for example). The thermal stability of QD field-effect transistors and solar cells built from ALD-infilled films is under evaluation in our laboratory.

Low-Temperature Aging. We also studied the effect of low temperatures on the aging behavior of our QD films in order to better understand the nature of the aging process in different gases. Films soaked in inert gas (nitrogen or helium) at low temperature show no changes in absorption spectra, presumably because the diffusive motion required for ripening and sintering is frozen out. For example, films of 3 nm QDs stored in the dark in nitrogen at 193 K (−80 °C freezer) showed no changes in absorption spectra after 1 month (Table 1). Likewise, UV-induced red shifting and broadening was completely absent after UV soaking in

flowing helium at 80 K (56 h soak at 3.5 mW cm^{-2}), whereas identical films soaked at 323 K showed typical red shifts (23 meV; Figure S11). The complete freeze out of optical changes at these relatively mild temperatures suggests that QD ripening and sintering are strongly activated processes (*i.e.*, large activation energies).

We also soaked films in dry oxygen to test whether QD oxidation could be suppressed at low temperature. Figure 8 shows a plot of peak energy and peak width for films of 7 nm QDs soaked for 50 h in UV light (3.5 mW cm^{-2}) and flowing oxygen at various temperatures (110−321 K). There are three salient features of the data. First, we cannot completely stop oxidation even at the lowest temperature (films soaked at 110 K still blue shift by ~25 meV). Films were found to oxidize at 110 K even in the dark (no UV). Second, the temperature dependence does not follow simple Arrhenius behavior. Instead, we observe a temperature-independent ~25 meV blue shift of the peak position at "low" temperatures (110−250 K) and a rapidly increasing blue shift at temperatures above 250 K. Time series show that the low-temperature blue shift occurs gradually during the UV soak. This behavior suggests the existence of two distinct stages of oxidation, with one stage dominant at low temperature and the second activated only at high temperature. We speculate that, at low temperature, oxidation is limited to the outermost monolayer of QD surface atoms. Once these atoms are oxidized (probably by chemisorption of oxygen), oxidation self-terminates and the blue shifting stops. At higher temperatures, however, there is sufficient thermal energy to activate solid-state diffusion and enable the oxidation of atoms deeper inside the QDs, resulting in a strong enhancement of the blue shift with temperature.

The third remarkable feature of the data in Figure 8 is the anomalously small and temperature-independent peak broadening, which averages only 7 meV across the temperature range (Figure 8b). In comparison, films that were UV-soaked at 323 K in air exhibited ~70 meV of broadening over the same period. We attribute the difference in peak broadening to the presence of moisture in air. This conclusion is based on the comparison of films UV-soaked at room temperature in dry oxygen *versus* humidified oxygen in a purpose-built environmental chamber. We observed five times more peak broadening in wet oxygen than in dry oxygen (22 meV *versus* 4 meV after 10 h of soaking), yet the blue shifts were very similar in the two environments (Figure S12). Enhanced peak broadening in the presence of moisture implies that water increases the QD size distribution without affecting the average QD size relative to UV soaking in dry oxygen. The explanation for this behavior is not clear, but it is possible that adsorbed water speeds oxidation of certain QD surface facets, resulting in greater size polydispersity for QD films oxidized in humid conditions.

To summarize, these low-temperature studies show that (*i*) UV-induced ripening and sintering of PbS QD films can be frozen out at low temperature but oxidation is only partially suppressed even at 110 K; (*ii*) oxidation follows a non-Arrhenius temperature dependence, with weakly activated, self-terminating surface oxidation at low temperature and strongly activated subsurface ("bulk") oxidation at high temperature; and (*iii*) moisture somehow increases the QD size distribution in photo-oxidized films without affecting the average QD diameter.

CONCLUSIONS

We have described the aging behavior of PbS QD films as a function of ambient atmosphere, temperature, UV illumination, and QD size. Aging in air causes oxidation and blue shifts of the first exciton peak in optical spectra, while aging in nitrogen results in ripening/sintering and red shifts in optical spectra. Both oxidation and ripening/sintering coarsen the QD size distribution and broaden the first exciton peak. Infilling and overcoating QD films with ALD alumina at room temperature produces inorganic nanocomposites in which external and internal diffusion are inhibited. The ALD coating serves both as a gas diffusion barrier that prevents oxidation and a 3D inorganic matrix that inhibits internal atomic and molecular motion. A 18 nm alumina overcoat completely prevents oxidation regardless of QD size, whereas the alumina matrix is most effective at stopping ripening/sintering of the larger QDs, which are easier to infill. TEM imaging of 7 nm QD monolayers revealed morphological changes consistent with the shifts observed in optical spectra. The ALD layers remain effective up to temperatures of ~100 °C, at which point they fail, apparently by reacting with the QDs.

We find that UV illumination causes preferential oxidation of large QDs but preferential ripening/sintering of small QDs. This difference is due to the greater driving force for ripening/sintering of smaller QDs. The main mechanism of UV action is not simple film heating; instead, it seems that UV-generated electron−hole pairs (*i*) cause photo-oxidation and (*ii*) create hotspots that trigger diffusion and ripening/sintering (particularly in small QDs). We can completely freeze out UV-induced ripening/sintering in inert gas by cooling films to 80 K, which suggests that ripening/sintering are strongly activated processes. However, UV-induced oxidation could not be eliminated even at temperatures as low as 110 K. From the temperature dependence, we identify two stages of oxidation, with self-terminating oxidation of the outermost monolayer of surface atoms occurring at low temperature and strongly activated subsurface oxidation important at higher temperature. We also find that

moisture is somehow responsible for most of the increase in size distribution of PbS QD films aged in air. Our results will be useful in ongoing efforts to fabricate truly stable QD films for next-generation solar cells.

METHODS

Chemicals. Lead oxide (PbO, 99.999%), oleic acid (OA, tech. grade, 90%), 1-octadecene (ODE, 90%), 1,2-ethanedithiol (EDT, >98%), trimethylaluminum (97%), and anhydrous solvents were purchased from Aldrich and used as received. Hexamethyldisilathiane (bis(trimethylsilyl) sulfide, TMS) was acquired from Gelest.

QD Synthesis. PbS QDs were synthesized using an air-free method modified from Hines and Scholes.[53] Briefly, PbO (2 mmol) was dissolved and degassed in OA (5 mmol) at 150 °C for ~1 h to form a lead oleate precursor solution. Next, a sulfur precursor solution containing 0.1 M TMS in ODE was rapidly injected into the flask at a specific injection temperature ranging from 120 to 150 °C to yield a dark-brown solution of PbS QDs. Isolation and purification were achieved by precipitating the QDs with ethanol and redispersing in hexane a total of four times, typically resulting in ~250 mg of QDs. Size control (2−7 nm diameter) was achieved by varying precursor concentration, injection temperature, and reaction time, yielding QDs with a relatively narrow size distribution of ~10%. Average size and size distribution were determined by analyzing 70−100 QDs in TEM images.

QD Film Deposition. QD films were prepared by dip coating onto glass substrates using a mechanical dip coater (DC Multi-4, Nima Technology) in a glovebox. Briefly, 1.2 × 1.2 cm^2 glass substrates were cleaned by acetone sonication and an ethanol rinse and dipped alternately into a 2 mg mL^{-1} solution of QDs in hexane and then a 2.5 mM solution of EDT in acetonitrile to make ~100 nm thick films. Film thickness was measured using tapping-mode atomic force microscopy (MFP-3D, Asylum Research) and SEM (FEI Quanta 3D FEG). Dip coating results in QD films on both sides of the glass. The QD film on the rear surface of each substrate was removed with a razor blade prior to stability testing.

Atomic Layer Deposition Infilling. QD films were coated with 15−20 nm of amorphous Al_2O_3 in a home-built cold-wall traveling wave ALD system built in a glovebox. Deposition was performed at 27 °C using alternating pulses of trimethylaluminum and water (40 ms pulse times, 60−120 s purge times, ~0.1 Torr base pressure). We have shown elsewhere[45] that this procedure fills the interstitial space of a PbX QD film with alumina (the first 1−4 nm) and subsequently overcoats the film with an alumina shell (see also Figure S1).

Characterization. Transmission electron microscopy was performed on a Philips CM 20 operating at 200 kV. Photoluminescence emission spectra of QD samples in TCE were acquired with a Shamrock 500 spectrometer equipped with an iDus InGaAs PDA detector (Andor Technologies) using 514 nm laser excitation. UV−vis absorption spectroscopy utilized a PerkinElmer Lambda 950 spectrophotometer and QD films mounted in air-tight optical cells consisting of two mated 1.33 in. UHV ConFlat sapphire viewports. Films mounted in these cells in the glovebox show no signs of oxidation even after months of storage in air.

For heat and UV soaking studies, QD films on glass substrates were placed directly on a hot plate or a hand-held UV lamp (1.4 mW cm^{-2} @ 365 nm; EL series lamps from UVP) either in air or in a glovebox (<5 ppm O_2 and H_2O). The temperature of samples sitting on the lamp was measured with a thermocouple to be ~50 °C. Periodically, each sample was sealed in an air-tight ConFlat cell for optical absorption measurements. A curve fitting program implemented in Origin 8.0 was used to extract the first exciton peak position and width.

Variable-temperature UV light soaking was performed on QD films mounted in an optical cryostat (ST-100 cryostat, Janis Research) inside of a glovebox and then transferred to the benchtop, evacuated, cooled, and backfilled with flowing helium or oxygen (5 N purity). A high-flux UV lamp (model B-100AP, UVP) was used to illuminate the films with 3.5 mW cm^{-2} of 365 nm light through a quartz window.

A homemade environmental testing chamber was used to deconvolute the effects of oxygen and moisture on QD films. Films were loaded into the air-tight chamber (constructed from a 4.5 in. CF flange, glass viewport, and valved gas lines) inside of a glovebox. Humidified gas was made by passing dry oxygen or nitrogen through a water bubbler prior to entering the test chamber. Films were illuminated with a hand-held UV lamp in the same geometry as described above. The gas flow rate was controlled with plug valves by monitoring the bubble rate of the exhaust flow.

For *ex situ* TEM studies, QD submonolayers were deposited on SiO_2 membrane window grids (25 nm thick windows, NanoBasic grids, Dune Sciences) using a single dip coating step and EDT treatment. Samples were imaged in the TEM immediately after fabrication, and fiduciary markers were used to relocate and monitor selected regions of each sample over time.

Acknowledgment. R.I. was supported by the Department of Energy under Award DE-SC0003904. J.T. acknowledges support from an NSF Graduate Research Fellowship. Y.L. and M.G. were supported by the Center for Advanced Solar Photophysics (CASP), an Energy Frontier Research Center funded by the U.S. Department of Energy (DOE), Office of Science, Office of Basic Energy Sciences (BES). We thank Craig Perkins for XPS data, Nathan Crawford for molecular size calculations, and the UCI School of Physical Sciences Center for Solar Energy for facilities support.

Supporting Information Available: Additional experimental details and figures. This material is available free of charge *via* the Internet at http://pubs.acs.org.

REFERENCES AND NOTES

1. Ridley, B. A.; Nivi, B.; Jacobson, J. M. All-Inorganic Field Effect Transistors Fabricated by Printing. *Science* **1999**, *286*, 746–749.
2. Morgan, N. Y.; Leatherdale, C. A.; Jarosz, M. V.; Drndic, M.; Kastner, M. A.; Bawendi, M. Electronic Transport in Films of Colloidal CdSe Nanocrystals. *Phys. Rev. B* **2002**, *66*, 075339.
3. Yu, D.; Wang, C.; Guyot-Sionnest, P. n-Type Conducting CdSe Nanocrystal Solids. *Science* **2003**, *300*, 1277–1280.
4. Talapin, D. V.; Murray, C. B. Nanocrystal Solids for n- and p-Channel Thin Film Field-Effect Transistors. *Science* **2005**, *310*, 86–89.
5. Kim, H.; Cho, K.; Kim, D. W.; Lee, H. R.; Kim, S. Bottom- and Top-Gate Field-Effect Thin-Film Transistors with p Channels of Sintered HgTe Nanocrystals. *Appl. Phys. Lett.* **2006**, *89*, 173107.
6. Porter, V. J.; Mentzel, T.; Charpentier, S.; Kastner, M. A.; Bawendi, M. G. Temperature-, Gate-, and Photoinduced Conductance of Close-Packed CdTe Nanocrystal Films. *Phys. Rev. B* **2006**, *73*, 155303.
7. Urban, J. J.; Talapin, D. V.; Shevchenko, E. V.; Kagan, C. R.; Murray, C. B. Synergism in Binary Nanocrystal Superlattices Leads to Enhanced p-Type Conductivity in Self-Assembled PbTe/Ag_2Te Thin Films. *Nat. Mater.* **2007**, *6*, 115–121.
8. Ginger, D. S.; Greenham, N. C. Charge Injection and Transport in Films of CdSe Nanocrystals. *J. Appl. Phys.* **2000**, *87*, 1361–1368.
9. Jarosz, M. V.; Porter, V. J.; Fisher, B. R.; Kastner, M. A.; Bawendi, M. G. Photoconductivity Studies of Treated CdSe Quantum Dot Films Exhibiting Increased Exciton Ionization Efficiency. *Phys. Rev. B* **2004**, *70*, 195327.
10. Oertel, D. C.; Bawendi, M. G.; Arango, A. C.; Bulovic, V. Photodetectors Based on Treated CdSe Quantum-Dot Films. *Appl. Phys. Lett.* **2005**, *87*, 213505.

11. Konstantatos, G.; Howard, I.; Fischer, A.; Hoogland, S.; Clifford, J.; Klem, E.; Levina, L.; Sargent, E. H. Ultrasensitive Solution-Cast Quantum Dot Photodetectors. *Nature* **2006**, *442*, 180–184.
12. Colvin, V. L.; Schlamp, M. C.; Alivisatos, A. P. Light-Emitting Diode Made from Cadmium Selenide Nanocrystals and a Semiconducting Polymer. *Nature* **1994**, *370*, 354–357.
13. Artemyev, M. V.; Sperling, V.; Woggon, U. Electroluminescence in Thin Solid Films of Closely Packed CdS Nanocrystals. *J. Appl. Phys.* **1997**, *81*, 6975–6977.
14. Gao, M.; Lesser, C.; Kirstein, S.; Mohwald, H.; Rogach, A. L.; Weller, H. Electroluminescence of Different Colors from Polycation/CdTe Nanocrystal Self-Assembled Films. *J. Appl. Phys.* **2000**, *87*, 2297–2302.
15. Coe, S.; Woo, W. K.; Bawendi, M.; Bulovic, V. Electroluminescence from Single Monolayers of Nanocrystals in Molecular Organic Devices. *Nature* **2002**, *420*, 800–803.
16. Bertoni, C.; Gallardo, D.; Dunn, S.; Gaponik, N.; Eychmüller, A. Fabrication and Characterization of Red-Emitting Electroluminescent Devices Based on Thiol-Stabilized Semiconductor Nanocrystals. *Appl. Phys. Lett.* **2007**, *90*, 034107.
17. Redl, F. X.; Cho, K.-S.; Murray, C. B.; O'Brien, S. Three-Dimensional Binary Superlattices of Magnetic Nanocrystals and Semiconductor Quantum Dots. *Nature* **2003**, *423*, 968–971.
18. Shevchenko, E. V.; Talapin, D. V.; Kotov, N. A.; O'Brien, S.; Murray, C. B. Structural Diversity in Binary Nanoparticle Superlattices. *Nature* **2006**, *439*, 55–59.
19. Shevchenko, E. V.; Talapin, D. V.; Murray, C. B.; O'Brien, S. Structural Characterization of Self-Assembled Multifunctional Binary Nanoparticle Superlattices. *J. Am. Chem. Soc.* **2006**, *128*, 3620–3637.
20. Nozik, A. J. Quantum Dot Solar Cells. *Physica E* **2002**, *14*, 115–120.
21. Klem, E. J. D.; MacNeil, D. D.; Cyr, P. W.; Levina, L.; Sargent, E. H. Efficient Solution-Processed Infrared Photovoltaic Cells: Planarized All-Inorganic Bulk Heterojunction Devices *via* Inter-Quantum-Dot Bridging during Growth from Solution. *Appl. Phys. Lett.* **2007**, *90*, 183113.
22. Luther, J. M.; Law, M.; Song, Q.; Reese, M. O.; Beard, M. C.; Ellingson, R. C.; Nozik, A. J. Schottky Solar Cells Based on Colloidal Nanocrystal Films. *Nano Lett.* **2008**, *8*, 3488–3492.
23. Koleilat, G. I.; Levina, L.; Shukla, H.; Myrskog, S. H.; Hinds, S.; Pattantyus-Abraham, A.; Sargent, E. H. Efficient, Stable Infrared Photovoltaics Based on Solution-Cast Colloidal Quantum Dots. *ACS Nano* **2008**, *2*, 833–840.
24. Law, M.; Beard, M. C.; Choi, S.; Luther, J. M.; Hanna, M. C.; Nozik, A. J. Determining the Internal Quantum Efficiency of PbSe Nanocrystal Solar Cells with the Aid of an Optical Model. *Nano Lett.* **2008**, *8*, 3904–3910.
25. Ma, W.; Luther, J. M.; Zheng, H. M.; Wu, Y.; Alivisatos, A. P. Photovoltaic Devices Employing Ternary PbS_xSe_{1-x} Nanocrystals. *Nano Lett.* **2009**, *9*, 1699–1703.
26. Choi, J. J.; Lim, Y. F.; Santiago-Berrios, M. B.; Oh, M.; Hyun, B. R.; Sung, L. F.; Bartnik, A. C.; Goedhart, A.; Malliaras, G. G.; Abruña, H. D.; *et al.* PbSe Nanocrystal Excitonic Solar Cells. *Nano Lett.* **2009**, *9*, 3749–3755.
27. Leschkies, K. S.; Beatty, T. J.; Kang, M. S.; Norris, D. J.; Aydil, E. S. Solar Cells Based on Junctions between Colloidal PbSe Nanocrystals and Thin ZnO Films. *ACS Nano* **2009**, *3*, 3638–3648.
28. Tsang, S.; Fu, H.; Ouyang, J.; Zhang, Y.; Yu, K.; Lu, J.; Tao, Y. Self-Organized Phase Segregation between Inorganic Nanocrystals and $PC_{61}BM$ for Hybrid High-Efficiency Bulk Heterojunction Photovoltaic Cells. *Appl. Phys. Lett.* **2010**, *96*, 243104.
29. Pattantyus-Abraham, A. G.; Kramer, I. J.; Barkhouse, A. R.; Wang, X.; Konstantatos, G.; Debnath, R.; Levina, L.; Raabe, I.; Nazeeruddin, M. K.; Grätzel, M.; *et al.* Depleted Heterojunction Colloidal Quantum Dot Solar Cells. *ACS Nano* **2010**, *4*, 3374–3380.
30. Luther, J. M.; Guo, J.; Lloyd, M. T.; Semonin, O. E.; Beard, M. C.; Nozik, A. J. Stability Assessment on a 3% Bilayer PbS/ZnO Quantum Dot Heterojunction Solar Cell. *Adv. Mater.* **2010**, *22*, 3704–3707.
31. Zhao, N.; Osedach, T. P.; Chang, L.; Geyer, S. M.; Wanger, D.; Binda, M. T.; Arango, A. C.; Bawendi, M. G.; Bulovic, V. Colloidal PbS Quantum Dot Solar Cells with High Fill Factor. *ACS Nano* **2010**, *4*, 3743–3752.
32. Debnath, R.; Tang, J.; Barkhouse, D. A. R.; Wang, X.; Pattantyus-Abraham, A. G.; Brzozowski, L.; Levina, L.; Sargent, E. H. Ambient-Processed Colloidal Quantum Dot Solar Cells *via* Individual Pre-encapsulation of Nanoparticles. *J. Am. Chem. Soc.* **2010**, *132*, 5952–5953.
33. Gao, J.; Luther, J. M.; Semonin, O. E.; Ellingson, R. J.; Nozik, A. J.; Beard, M. C. Quantum Dot Size Dependent $J-V$ Characteristics in Heterojunction ZnO/PbS Quantum Dot Solar Cells. *Nano Lett.* **2011**, *11*, 1002–1008.
34. Tang, J.; Brzozowski, L.; Barkhouse, D. A. R.; Wang, X. H.; Debnath, A. J.; Wolowiec, R.; Palmiano, E.; Levina, L.; Pattantyus-Abraham, A. G.; Jamakosmanovic, D.; *et al.* Quantum Dot Photovoltaics in the Extreme Quantum Confinement Regime: The Surface-Chemical Origins of Exceptional Air- and Light-Stability. *ACS Nano* **2010**, *4*, 869–878.
35. Tang, J.; Wang, X. H.; Brzozowski, L.; Barkhouse, D. A. R.; Debnath, R.; Levina, L.; Sargent, E. H. Schottky Quantum Dot Solar Cells Stable in Air under Solar Illumination. *Adv. Mater.* **2010**, *22*, 1398–1402.
36. Peterson, J. J.; Krauss, T. D. Photobrightening and Photodarkening in PbS Quantum Dots. *Phys. Chem. Chem. Phys.* **2006**, *8*, 3851–3856.
37. Stouwdam, J. W.; Shan, J.; van Veggel, F. C. J. M.; Pattantyus-Abraham, A. G.; Young, J. F.; Raudsepp, M. Photostability of Colloidal PbSe and PbSe/PbS Core/Shell Nanocrystals in Solution and in the Solid State. *J. Phys. Chem. C* **2007**, *111*, 1086–1092.
38. Dai, Q.; Wang, Y.; Zhang, Y.; Li, X.; Li, R.; Zou, B.; Seo, J. T.; Wang, Y.; Liu, M.; Yu, W. W. Stability Study of PbSe Semiconductor Nanocrystals over Concentration, Size, Atmosphere, and Light Exposure. *Langmuir* **2009**, *25*, 12320–12324.
39. Sykora, M.; Koposov, A. Y.; McGuire, J. A.; Schulze, R. K.; Tretiak, O.; Pietryga, J. M.; Klimov, V. I. Effect of Air Exposure on Surface Properties, Electronic Structure, and Carrier Relaxation in PbSe Nanocrystals. *ACS Nano* **2010**, *4*, 2021–2034.
40. Dai, Q.; Zhang, Y.; Wang, Y.; Wang, Y.; Zou, B.; Yu, W. W.; Hu, M. Z. Ligand Effects on Synthesis and Post-synthetic Stability of PbSe Nanocrystals. *J. Phys. Chem. C* **2010**, *114*, 16160–16167.
41. Luther, J. M.; Law, M.; Song, Q.; Perkins, C. L.; Beard, M. C.; Nozik, A. Structural, Optical, and Electrical Properties of Self-Assembled Films of PbSe Nanocrystals Treated with 1,2-Ethanedithiol. *ACS Nano* **2008**, *2*, 271–280.
42. Law, M.; Luther, J. M.; Song, Q.; Hughes, B. K.; Perkins, C. L.; Nozik, A. J. Structural, Optical, and Electrical Properties of PbSe Nanocrystal Solids Treated Thermally or with Simple Amines. *J. Am. Chem. Soc.* **2008**, *130*, 5974–5985.
43. Zarghami, M. H.; Liu, Y.; Gibbs, M.; Gebremichael, E.; Webster, C.; Law, M. p-Type PbSe and PbS Quantum Dot Solids Prepared with Short-Chain Acids and Diacids. *ACS Nano* **2010**, *4*, 2475–2485.
44. Leschkies, K. L.; Kang, M. S.; Aydil, E. S.; Norris, D. J. Influence of Atmospheric Gases on the Electrical Properties of PbSe Quantum-Dot Films. *J. Phys. Chem. C* **2010**, *114*, 9988–9996.
45. Liu, Y.; Gibbs, M.; Perkins, C. L.; Tolentino, J.; Zarghami, M. H.; Law, M. In press.
46. van Huis, M. A.; Kunneman, L. T.; Overgaag, K.; Xu, Q.; Pandraud, G.; Zandbergen, H. W.; Vanmaekelbergh, D. Low-Temperature Nanocrystal Unification through Rotations and Relaxations Probed by *In Situ* Transmission Electron Microscopy. *Nano Lett.* **2008**, *8*, 3959–3963.
47. Schapotschnikow, P.; van Huis, M. A.; Zandbergen, H. W.; Vanmaekelbergh, D.; Vlugt, T. J. H. Morphological Transformations and Fusion of PbSe Nanocrystals Studied Using Atomistic Simulations. *Nano Lett.* **2010**, *10*, 3966–3971.
48. Lee, B.; Podsiadlo, P.; Rupich, S.; Talapin, D. V.; Rajh, T.; Shevchenko, E. V. Comparison of Structural Behavior of Nanocrystals in Randomly Packed Films and Long-Range

Ordered Superlattices by Time-Resolved Small Angle X-ray Scattering. *J. Am. Chem. Soc.* **2009**, *131*, 16386–16388.
49. Mentzel, T. S.; Porter, V. J.; Geyer, S.; MacLean, K.; Bawendi, M. G.; Kastner, M. A. Charge Transport in PbSe Nanocrystal Arrays. *Phys. Rev. B* **2008**, *77*, 075316.
50. Turyanska, L.; Elfurawi, U.; Li, M.; Fay, M. W.; Thomas, N. R.; Mann, S.; Blokland, J. H.; Christianen, P. C. M.; Patané, A. Tailoring the Physical Properties of Thiol-Capped Pbs Quantum Dots by Thermal Annealing. *Nanotechnology* **2009**, *20*, 315604.
51. Lü, W.; Yamada, F.; Kamiya, I. Fabrication and Coupling Investigation of Films of PbS Quantum Dots. *J. Vac. Sci. Technol., B* **2010**, *28*, C5E8–C5E12.
52. Smith, B. B.; Nozik, A. J. Theoretical Studies of Electronic State Localization and Wormholes in Silicon Quantum Dot Arrays. *Nano Lett.* **2001**, *1*, 36–41.
53. Hines, M. A.; Scholes, G. D. Colloidal PbS Nanocrystals with Size-Tunable Near-Infrared Emission: Observation of Post-synthesis Self-Narrowing of the Particle Size Distribution. *Adv. Mater.* **2003**, *15*, 1848–1849.
54. Moreels, I.; Lambert, K.; Smeets, D.; De Muynck, D.; Nollet, T.; Martins, J. C.; Vanhaecke, F.; Vantomme, A.; Delerue, C.; Allan, G.; Hens, Z. Size-Dependent Optical Properties of Colloidal PbS Quantum Dots. *ACS Nano* **2009**, *3*, 3023–3030.
55. Gao, J.; Perkins, C. L.; Luther, J. M.; Hanna, M. C.; Chen, H.; Semonin, O. E.; Nozik, A. J.; Ellingson, R. J.; Beard, M. C. n-Type Transition Metal Oxide as a Hole Extraction Layer in PbS Quantum Dot Solar Cells. *Nano Lett.* **2011**, *11*, 3263–3266.
56. Groner, M. D.; Fabreguette, F. H.; Elam, J. W.; George, S. M. Low-Temperature Al_2O_3 Atomic Layer Deposition. *Chem. Mater.* **2004**, *16*, 639–645.
57. Luo, Y.; Slater, D.; Han, M.; Moryl, J.; Osgood, R. M. Low-Temperature, Chemically Driven Atomic-Layer Epitaxy: *In Situ* Monitored Growth of CdS/ZnSe(100). *Appl. Phys. Lett.* **1997**, *71*, 3799–3801.
58. Knez, M.; Kadri, A.; Wege, C.; Gösele, U.; Jeske, H.; Nielsch, K. Atomic Layer Deposition on Biological Macromolecules: Metal Oxide Coating of Tobacco Mosaic Virus and Ferritin. *Nano Lett.* **2006**, *6*, 1172–1177.
59. Klaus, J. W.; Sneh, O.; George, S. M. Growth of SiO_2 at Room Temperature with the Use of Catalyzed Sequential Half-Reactions. *Science* **1997**, *278*, 1934–1936.
60. Liang, X. H.; King, D. M.; Li, P.; Weimer, A. W. Low-Temperature Atomic Layer-Deposited TiO_2 Films with Low Photoactivity. *J. Am. Ceram. Soc.* **2009**, *92*, 649–654.
61. Meyer, J.; Schneidenbach, D.; Winkler, T.; Hamwi, S.; Weimann, T.; Hinze, P.; Ammermann, S.; Johannes, H.-H.; Riedl, T.; Kowalsky, W. Reliable Thin Film Encapsulation for Organic Light Emitting Diodes Grown by Low-Temperature Atomic Layer Deposition. *Appl. Phys. Lett.* **2009**, *94*, 233305.
62. Hyde, G. K.; McCullen, S. D.; Jeon, S.; Stewart, S. M.; Jeon, H.; Loboa, E. G.; Parsons, G. N. Atomic Layer Deposition and Biocompatibility of Titanium Nitride Nano-coatings on Cellulose Fiber Substrates. *Biomed. Mater.* **2009**, *4*, 025001.
63. Knez, M.; Niesch, K.; Niinisto, L. Synthesis and Surface Engineering of Complex Nanostructures by Atomic Layer Deposition. *Adv. Mater.* **2007**, *19*, 3425–3438.
64. Nanu, M.; Schoonman, J.; Goossens, A. Inorganic Nanocomposites of n- and p-Type Semiconductors: A New Type of Three-Dimensional Solar Cell. *Adv. Mater.* **2004**, *16*, 453–456.
65. Pourret, A.; Guyot-Sionnest, P.; Elam, J. W. Atomic Layer Deposition of ZnO in Quantum Dot Thin Films. *Adv. Mater.* **2009**, *21*, 232–235.
66. Molecular geometry optimized with Turbomole at TPSS/def2-TZVP quality. The size is determined by adding vdW radii to the internuclear distances.